Small-angle x-ray-scattering study of silver-nanocrystal disorder-order phase transitions

Brian A. Korgel* and Donald Fitzmaurice†
Department of Chemistry, University College Dublin, Belfield, Dublin 4, Ireland
(Received 1 June 1998; revised manuscript received 25 September 1998)

A conceptually unique approach was developed to study the interparticle interactions between organized alkanethiol-capped silver nanocrystals. Dense nanocrystal fluids were formed by evaporating the solvent from a ''size-polydisperse'' ($\sigma \cong \pm 12\%$) nanocrystal dispersion on a substrate. The sample polydispersity prevented the disorder-order phase transition (i.e., superlattice formation) from occurring. Small-angle x-ray scattering was then used to measure the static structure factors $S(q)$, of these disordered nanocrystal films as a function of the ratio $\langle L \rangle / R$ between the capping ligand chain length to the core nanocrystal radius. The pair-distribution and direct correlation functions were then calculated from Fourier transformations of $S(q)$. This enabled the use of the hypernetted chain approximation to calculate the pair interparticle potential $u(r)$. The 6-12 Lennard-Jones potential provided reasonable fits to all experimentally determined values of $u(r)$, indicating the predominance of relatively short-range repulsion between nanocrystals. Monodisperse dodecanethiol- and octanethiol-capped silver nanocrystals were then condensed into ordered arrays. Face-centered-cubic (fcc) packing was favored for $\langle L \rangle / R < 0.60$, and body-centered-cubic (bcc) packing was favored when $\langle L \rangle / R > 0.60$. Lower-symmetry body-centered-tetragonal packing was observed for octanethiol-capped silver nanocrystals with $\langle L \rangle / R > 0.66$. A simple model employing the experimentally determined values for $u(r)$, predicts that the fcc→bcc superlattice phase transition occurs when $\langle L \rangle / R \cong 0.65$.
[S0163-1829(99)13421-0]

I. INTRODUCTION

The ability to assemble organized arrays of semiconductor or metal quantum dots with precise control over the dot and interdot dimensions is of growing interest since these mesoscopic materials often exhibit physical properties that differ from natural bulk materials and could lead to the development of a diverse set of new technologies, ranging from coatings, electronics, magnetics, separations, and adhesives. Recently, several groups have proved that quantum dot superlattices can be constructed with tunable nanometer-scale dot and interdot dimensions by spin-coating dispersions of sterically stabilized nanocrystals on a suitable substrate.[1–15] This approach has been shown to be quite general and has been applied to a variety of semiconductor and metal materials, including γ-Fe_2O_3,[1] CdSe,[2,3] Ag,[5,11,13,14] Au,[4,6–9,12] Ag_2S,[10] and CoO.[15]

Fundamental interest in these nanocrystal arrays largely stems from the unique size-dependent optical, electronic, and/or magnetic properties of the individual nanocrystals that result from their small size (<100 Å diameter).[16] The ability to condense nanocrystals onto solid supports might further their characterization by enabling many of the solid-state techniques developed to study thin films to be applied to the study of nanocrystal properties. These arrays also provide the opportunity to study collective physical behavior resulting from interactions between neighboring dots, since interdot spacings are on the order of only 10 Å. In these situations, the superlattice structure may significantly affect the physical properties of the nanocrystal array (for example, see Ref. 3), which motivates the need for a fundamental understanding of nanocrystal self-organization. Currently, however—even though nanocrystal self-organization is the only proven method for achieving these structures with dimensions at least one order of magnitude smaller than those possible using lithographic techniques—there exists little more than an empirical sense of how nanocrystals self-organize.

The material properties that appear to enable nanocrystals to form superlattices are sufficient steric stabilization provided by capping ligands [e.g., dodecanethiol ($C_{12}H_{25}SH$), see Fig. 1] and a narrow particle size (and shape) distribution. As the solvent evaporates from the dispersion on a substrate, the nanocrystal volume fraction increases, eventually reaching the point where the nanocrystals lock into place. Since nanocrystals diffuse rapidly due to their small size, they can sample a very large number of configurations during solvent evaporation, and can thus, essentially achieve their lowest energy structures. Therefore, both the disordered

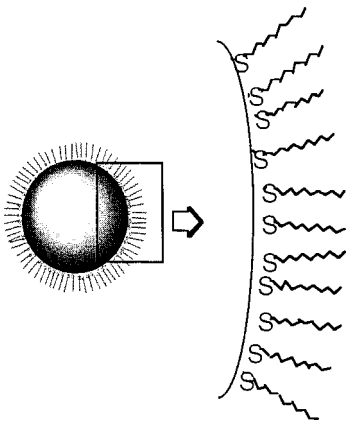

FIG. 1. Silver nanocrystal coated with a dodecanethiol monolayer. The thiol chemisorbs to the silver surface resulting in the formation of a hydrophobic shell of alkane chains that prevent irreversible aggregation. The capping layer density determines the interparticle spacing in the condensed superlattice.

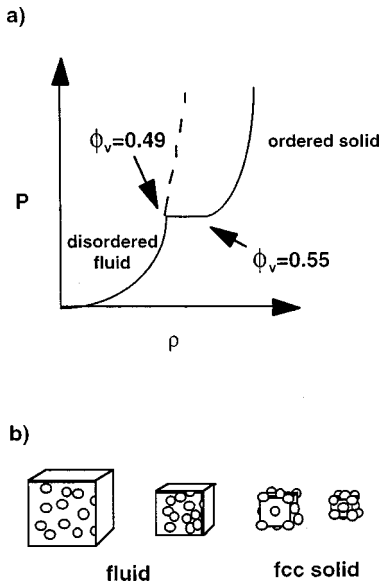

FIG. 2. (a) Thermodynamic pressure plotted versus particle density as depicted in (b) for a dispersion of hard spheres as calculated using molecular-dynamics simulations (Refs. 21,22). As solvent evaporates from the dispersion the volume decreases resulting in increased ϕ_v, thus increasing P. When a monodisperse collection of (fluid) particles reach $\phi_v = 0.49$, it undergoes the so-called Kirkwood-Alder disorder-order phase transition to an fcc solid. Reentrant melting occurs at $\phi_v = 0.55$. A collection of particles with a standard deviation about the mean diameter much above 10% will remain the fluid phase (no order), as depicted by the dashed curve in (a).

dispersion and the ordered superlattice can be described using statistical thermodynamic models of fluids and solids.

The important parameter in these models is the pair interaction potential V_{ij}, between two isolated nanocrystals i and j, separated by a distance r. This parameter is explicitly related to the free energy F of a given phase:

$$F = -\frac{1}{\beta}\ln\left[\sum_{\substack{\text{arrangement}\\ \text{of nanocrystals}}} \exp\left(-\sum_{i,j,\text{interactions}} \beta V_{ij}\right)\right], \quad (1)$$

where $\beta = 1/kT$.[17,18] Therefore, with V_{ij} known, the most stable structures can be determined *a priori* by calculating F. (It should be noted, however, that even when V_{ij} is known, calculating F is in most cases not trivial and the study of phase transitions of molecular liquids and solids is still an active area of research.) For example, if nanocrystals interact like hard spheres, then the experimentally observed nanocrystal ordering could simply be described as a Kirkwood-Alder transition from a disordered fluid (dispersion) to an ordered solid (superlattice) and the most stable superlattice structure would be face-centered-cubic (fcc) (Fig. 2).[11,19–22] These nanocrystals, however, do not behave like hard spheres.[8,9,12,14,23,24]

The soft organic capping ligand shell occupies a volume significant compared to the core volume and must be considered. Some have proposed that very strong interactions occur between stabilizing ligands within the superlattice.[8,9,25] Although this has not been confirmed experimentally, the chains certainly fill the interstitial space in the superlattice and the nanocrystals pack as ''soft spheres'' with an ''effective hard-sphere'' diameter that encompasses both the inorganic core and the organic capping layer.[14] Furthermore, the dispersion energy between nanocrystals appears to result in a net weak attraction between particles, particularly in the case of metal nanocrystals which have a high Hamaker constant. This attraction leads to ordering phenomena qualitatively different from what would be expected for hard spheres: for example, the formation of opals of polydisperse gold nanocrystals;[23] the ability to control the thickness of nanocrystal films by varying the solvent polarity;[12] the preferred formation of body-centered-cubic (bcc) superlattices for gold nanocrystals with high ratios of capping ligand chain length to core particle diameter;[8,9] and negative pressure-area isotherms for silver nanocrystal monolayers present at the air-water interface on a Langmuir-Blodgett trough.[24] The attraction also appears to aid the ordering process by pulling nanocrystals close to their entropically favored (at high volume fractions) lattice position in the superlattice.[14] Therefore, in order to understand nanocrystal self-organization, the interparticle interactions must be understood.

Small-angle x-ray-scattering (SAXS) measurements can probe both the structure of individual dispersed nanocrystals [the shape factor, $P(\theta)$] and the superstructure of condensed nanocrystal arrays [the static structure factor, $S(\theta)$], with the scattered x-ray intensity $I(\theta) \propto P(\theta)S(\theta)$.[2,3,8,9,11,14,26–28] For noninteracting particles $S(\theta) = 1$. But for concentrated fluids and solids, $S(\theta) \neq 1$ and $S(\theta)$ reveals the superstructure and the degree of ordering. For an ordered solid, $S(\theta)$ exhibits features characteristic of a periodic array with long-range order, whereas, features characteristic of short-range order develop for a dense fluid. A number of statistical mechanical methods have been proposed for liquids (disordered fluids) that relate the experimentally measurable quantity $S(\theta)$ to V_{ij}, and vice-versa.[18,29] These methods rely on the use of the pair-distribution function $g(r)$, and the direct correlation function $c(r)$, and have been applied to the study of various supermolecular structural problems, including noble gas liquids,[30] ordered diblock copolymer micelles,[31] and disordered (or amorphous) metals for structural determination.[32,33] Therefore, the aim of this paper is to determine V_{ij} using small-angle x-ray scattering in order to elucidate its importance to nanocrystal self-organization.

The approach adopted was to determine V_{ij} experimentally [hereafter denoted $u(r)$], by performing SAXS measurements on dense disordered nanocrystal fluids. Very dense nanocrystal fluids were experimentally accessed by condensing a slightly polydisperse nanocrystal dispersion onto a substrate. By incorporating a size distribution with a standard deviation about the mean diameter slightly larger than the maximum value of ~10% required to achieve ordering, the ordering phase transition typical for size-monodisperse nanocrystals upon solvent evaporation does not occur.[34,35] The nanocrystal film can, therefore, be conceived of as a very viscous disordered fluid or as an amorphous solid. Consequently, models developed for molecular liquids which relate $S(\theta)$ and $u(r)$ were applied to nanocrystal systems.

II. EXPERIMENT

A. Nanocrystal preparation and characterization

Silver nanocrystals capped with alkanethiols ($C_8H_{17}SH$ and $C_{12}H_{25}SH$) were prepared by arrested precipitation using

standard methods.[11,13,14,36] In a typical experiment, an aqueous solution of silver ions (0.15 g $AgNO_3$ in 30 ml pure water) was added to chloroform containing the phase transfer catalyst, tetraoctylammonium bromide [$(C_8H_{17})_4NBr$, 2.23 g in 20.4 ml chloroform]. The organic phase was then collected. The silver ions were subsequently reduced with $NaBH_4$ (0.39 g in 24 ml pure water) in the presence of the thiol (8×10^{-3} mol). The thiol stabilizes the growing colloids by binding to the nanocrystal surface and helps to maintain a relatively narrow particle size distribution. The resulting colloidal dispersion was washed with ethanol to remove all the phase transfer catalyst and any unbound thiol.

The nanocrystal size distribution was narrowed by size selective precipitation using chloroform/ethanol as the solvent/nonsolvent pair.[2,11,13,14] Ethanol was added dropwise to the nanocrystal dispersion until opalescence persisted. The opalescence results from the agglomeration of only the largest particles in the dispersion, which were collected by centrifugation. A series of precipitations from a single preparation enabled the isolation of nanocrystals with decreasing average radius. The polydisperse sample was isolated by overtitrating the dispersion with polar solvent slightly past the endpoint typically used for monodisperse samples. The alkanethiol-capped silver nanocrystals redisperse in a variety of organic solvents, including chloroform, hexane, and toluene.

Transmission electron microscopy (TEM) using a JEOL JEL-2000 EX electron microscope with a 200 kV accelerating voltage (lattice resolution of 0.14 nm and point-to-point resolution of 0.3 nm) was used to characterize nanocrystal monolayers spin coated onto carbon-coated copper grids. Characterization of the organic capping with ^{1}H NMR (using a JEOL JNM-GX270 FT spectrometer at 20 °C), and Fourier-transform infrared spectroscopy (using a Mattson Galaxy 3000 FT spectrometer with CaF_2 windows, and a 0.20 mm path length at 20 °C), and elemental analysis, confirmed that a close-packed monolayer of alkanethiols surround each nanocrystal.[14]

B. Small-angle x-ray scattering

SAXS measurements were performed on beam line 8.2 of the Synchrotron Radiation Source at the Daresbury Laboratory, Warrington, U.K, with monochromatic radiation of wavelength $\lambda = 1.54$ Å. Scattered photons were collected on a multiwire gas-filled quadrant detector. The scattering angle was calibrated using an oriented specimen of wet collagen (rat-tail tendon). The incident radiation intensity was recorded using a parallel plate ionization detector located before the sample cell. All experimental data were corrected for background scattering, sample absorption, and the positional alinearity of the detector.

SAXS measurements were collected for hexane-dispersed alkanethiol-capped silver nanocrystals (1–5 mg/ml) and silver nanocrystal (optically transparent) thin films. The films were formed by spin coating a mica substrate with 0.2 ml of a 7 mg/ml dispersion of nanocrystals in hexane at room temperature (20 °C).

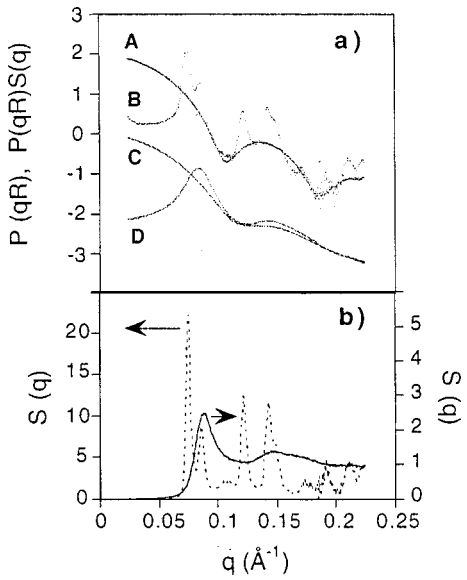

FIG. 3. (a) Shape factors $[P(qR)]$ measured for two different hexane-dispersed dodecanethiol-capped silver nanocrystal samples: curve (A) $\overline{R}=41$ Å ($\pm6.8\%$); curve (C) $\overline{R}=36$ Å ($\pm14.4\%$). $S(q)=1$ in these dispersions. Curves (B) and (D) are the corresponding normalized diffraction patterns [i.e., plotting $P(qR)S(q)$] for these nanocrystal samples spin-coated onto mica substrates. Curves (A) and (C) are offset by a factor of 100. (b) Structure factors $[S(q)]$ determined from diffraction patterns (B), (– – –), and (D), (——), in Fig. 3(a).

III. RESULTS AND DISCUSSION

A. SAXS measurements: The size distribution and superstructure

From a collection of hydrocarbon-coated silver nanocrystals, the silver cores can be considered as the sole source of the x-ray scattering signal since the electron density difference between the alkane capping ligands and hexane is minimal. The intensity of radiation scattered $I(\theta)$, relates proportionally to the shape factor $P(\theta)$ and the static structure factor $S(\theta)$: $I(\theta)\propto P(\theta)S(\theta)$.[26,28] By first measuring $P(\theta)$ for dilute noninteracting particle dispersions, $S(\theta)$ can subsequently be determined for concentrated nanocrystal thin films.

The analytical expression for $P(\theta)$ for a sphere is[26,37]

$$P(\theta)=P(qR)=\left[3\,\frac{\sin(qR)-qR\cos(qR)}{(qR)^3}\right]^2, \qquad (2)$$

with the wave vector q, defined as $q=(4\pi/\lambda)\sin(\theta)$, where θ is the scattering angle 2θ. (q is inversely proportional to the characteristic d spacing in the system: $d=2\pi/q$.) For a polydisperse sample, the size distribution, $n(R)/n_{\text{total}}$, affects $I(q)$:[26,37]

$$I(q)\propto\int_0^\infty\left(\frac{n(R)}{n_{\text{total}}}\right)P(qR)R^6dR. \qquad (3)$$

The shape of the size distribution must be assumed in order to calculate the average particle radius $\overline{R}$, and the standard deviation σ, from the SAXS data. A Gaussian distribution

$$\frac{n(R)}{n_{\text{total}}} = \frac{1}{\sigma\sqrt{2\pi}} \exp\left[\frac{-(R-\overline{R})^2}{2\sigma^2}\right], \tag{4}$$

was assumed for all curve fits.

Curves (A) and (C) in Fig. 3(a) show $P(qR)$ measured from dilute hexane dispersions of monodisperse and polydisperse dodecanethiol-capped silver nanocrystals, respectively (1 mg/ml). These curves are characteristic of noninteracting particles and the position of the maxima in the oscillations in curves (A) and (C) in Fig. 3(a) correspond roughly to the average nanocrystal radius, while the intensity of the oscillations corresponds to the size distribution. For example, $\overline{R}$ is larger for curve (A) than curve (C) and σ is smaller. Curves such as these were fitted with Eqs. (2)–(4) to determine $\overline{R}$ and σ for all of the samples examined in this study (see Tables I and II and the associated discussion below).

Mica substrates were then spin coated with the nanocrystals to form a transparent violet film. Curves (B) and (D) in Fig. 3(a) show the measured values of $P(qR)S(q)$ for these films. Since the curves differ from curves (A) and (C), it is clear that $S(q) \neq 1$. Both curves (B) and (D) show decreased scattering at low q accompanied by distinct peaks at higher q resulting from destructive and constructive interference due to ordering in the film. Therefore, both samples exhibit some degree of order.

The sharp diffraction peaks in $S(q)$ for the monodisperse sample reach values close to 25 [Fig. 3(b)] and index to an fcc superlattice with an interparticle separation of 15.9 Å. In contrast, the SAXS pattern for the polydisperse nanocrystal film in Fig. 3(b) displays only two peaks in $S(q)$ with longer range oscillations characteristic of liquids, where short-range ordering occurs due to excluded volume effects. The TEM images in Fig. 4, compare such ordered and disordered nanocrystal thin films, and establish that the polydisperse nanocrystals pack as an open network, which is clearly different from that of the highly compact hexagonal close-packed monolayer formed with monodisperse nanocrystals. Furthermore, the broad diffraction peaks exhibited by the polydisperse sample cannot be indexed simply as an fcc lattice with a large positional distribution.

The SAXS data in Fig. 3, corroborated with the TEM images in Fig. 4, indicate that the structures of the condensed films formed from monodisperse and polydisperse samples are qualitatively different. It should be noted that the difference in size distribution between these two samples is only 7.6%. The polydisperse samples ($\sigma = \pm 14.4\%$) still exhibit distinct oscillations in $P(qR)$, which typically characterize reasonably monodisperse colloidal dispersions. However, the polydisperse sample has not undergone the fluid-solid phase transition, which means that $S(q)$ may be determined for dense nanocrystal fluids.

The following section presents the experiments in which polydisperse samples were condensed into thin films, $S(q)$ was measured, and then $u(r)$ was calculated from $S(q)$ using available statistical models for fluids.

B. Disordered dense nanocrystal films

A series of six dodecanethiol-capped silver nanocrystal samples with differing average core diameters were isolated from consecutive size-selective precipitations. The SAXS patterns of these samples dispersed in hexane are shown in Fig. 5(a). Fitting Eqs. (2)–(4) to curves A–F determined the values of $\overline{R}$ and σ listed in Table I. $\overline{R}$ decreased by approximately 3.2 Å with each precipitation and σ had an average value of $\pm 13\%$.

After measuring $P(qR)$, the nanocrystals were spin coated onto mica substrates. Figure 5(b) shows $S(q)$ for these films. The diffraction peaks cannot be indexed to an fcc lattice and $S(q)$ oscillates around a value close to 1, indicating short-range order in the samples. Despite the size distribution, the first-order diffraction peak shifts predictably to higher q with decreasing core size.

The corresponding radial distribution functions $g(r)$, are plotted in Fig. 6(a). $g(r)$ indicates the probability of finding another particle at a distance r, from the center of a central particle and is calculated from a Fourier transformation of $S(q)$:[29]

$$g(r) = 1 + \frac{1}{2\pi^2 \rho r} \int q(S(q)-1)\sin(qr)\,dq. \tag{5}$$

The particle number density ρ, was estimated by assuming a closest-packed disordered fluid with $\phi_v = 0.68$.[35] Without considering the size distribution, $\rho = \phi_v / [\frac{4}{3}\pi(\overline{R} + \delta/2)^3]$. The denominator represents the volume occupied per particle, which includes the portion of the capping ligands that keep the nanocrystals separated in the film. The effect of the size distribution on ρ was accounted for in the calculations by assuming a Gaussian distribution, using $\overline{R}$ and $\delta = 13.9$ Å (discussed below) as determined from the SAXS measurements:

TABLE I. Average size and size distribution for the polydisperse dodecanethiol-capped silver nanocrystals determined by fitting Eqs. (2)–(4) to the SAXS data in Fig. 5(a) for hexane dispersions. Also shown is the film density calculated using Eq. (6) and the best-fit parameters for $u(r)$ in Fig. 8.

Sample	$\overline{R}$ (Å)	σ	ρ ($\times 10^6$ Å^{-3})	σ_{LJ} (Å)	ε (kT)	A (eV)	δ_{SAM}
A	36	5.2(14.4%)	0.8	80.0	5.6	7.8	15
B	33	4.1(12.4%)	1.1	74	4.6	7.8	15
C	29	3.5(12.1%)	1.6	67	2.5	7.8	15
D	25	2.5(10%)	2.5	68	2.7	7.8	13
E	23	3.1(13.5%)	3.2	60	1.3	3	10
F	20	3.5(17.5%)	4.7	52	0.9	1.5	7

$$\rho = 0.68 \frac{\int \frac{1}{\sigma\sqrt{2\pi}} \exp[-(R-\bar{R})^2/2\sigma^2]\,dR}{\int \{(1/\sigma\sqrt{2\pi})\exp[-(R-\bar{R})^2/2\sigma^2]\} \times [(4\pi/3)(R+\delta/2)^3]\,dR}. \quad (6)$$

This number density represents an upper limit and affects only the magnitude of $g(r)$. Estimating ρ using a lower limit of $\phi_v = 0.55$, which is representative of the reentrant melting for hard spheres,[22] increases the maximum value of $g(r)$ by ~8% at most.

The regular oscillations occurring in $g(r)$ indicate liquidlike structure. Some evidence of longer-range structural order occurs in samples A and D in Fig. 6(a) with the second and third peaks slightly coupled as might be found in a near-fcc crystal[38] or a glass.[33] However, the values of the maxima of $g(r)$ are very low, indicating a low coordination number.[28,29] $g(r)$ for the other samples oscillates as expected for fluids. The first peak in $g(r)$ in Fig. 6(a) corresponds to the center-to-center interparticle distance. The surface-to-surface interparticle spacing (δ) between these nanocrystals does not depend on particle diameter and has an average value for the six samples of 13.9 Å. This value is slightly less than the average interparticle spacing measured between dodecanethiol-capped silver nanocrystals in fcc superlattices.[11,14] The smaller interparticle spacing in the fluid results from the lower coordination between particles which forces the capping ligands to fill more space, thus decreasing the ''screening length'' between particles.

By using the theories developed for molecular liquids, $u(r)$ was calculated from $S(q)$. In a liquid, many-body effects are important and must be accounted for when relating $u(r)$—for two *isolated* species—to the liquid structure measured using SAXS. Correlation functions have been developed to relate $u(r)$ to the potential felt between two particles in the presence of N-2 other particles, $w(r)$. The total correlation function, $h(r) = g(r) - 1$ can be decomposed into direct and indirect contributions, $c(r)$ and $\gamma(r)$, respectively, using the Ornstein-Zernike equation,

$$h(r_{12}) = \gamma(r_{12}) + c(r_{12}) = c(r_{12}) + \rho \int c(r_{23}) h(r_{13})\,dr_3, \quad (7)$$

where the subscripts denote the species in the fluid.[29] The Fourier transformations of $h(r)$ $[H(q) = S(q) - 1]$, the Ornstein-Zernike equation $[H(q) = C(q) + \rho C(q) H(q)]$, and $c(r)$ $[C(q) = \rho \int c(r) e^{iq\cdot\mathbf{r}} d\mathbf{r}]$, can be employed to calculate $c(r)$ from $S(q)$:[18,29]

$$c(r) = \frac{1}{4\pi\rho r} \int q \left(\frac{S(q)-1}{S(q)} \right) \sin(qr)\,dq. \quad (8)$$

Figure 6(b) shows $c(r)$ calculated for the dense nanocrystal fluids examined in Figs. 5 and 6(a). $c(r)$ varies more slowly with r than $g(r)$, as expected.

After calculating the correlation functions from experimentally measured values of $S(q)$, $u(r)$ was calculated using the hypernetted-chain (HNC) approximation[18,29]

$$\beta u(r) = g(r) - 1 - c(r) - \ln[g(r)]. \quad (9)$$

The HNC approximation was chosen since it appears to best describe the properties of dense fluids, such as the one-component plasma.[39] Figures 7 and 8 show $u(r)$ calculated for the nanocrystal fluids examined in Figs. 5 and 6. An attractive energy minimum appears for all core particle diameters. This attraction decreases with decreased particle size, as expected for a series of particles capped with the same ligands.[12,14]

One estimate of $u(r)$ for these sterically stabilized nanocrystals is the sum of the van der Waals attraction and the steric repulsion:[38]

$$u(r) = E_{\text{steric}} + E_{\text{vdW}}. \quad (10)$$

E_{steric} can be calculated using the expression developed by de Gennes for a tightly packed monolayer in a good solvent:[40–42]

TABLE II. Average sizes and size distributions for monodisperse dodecanethiol-capped (C_{12}) (samples i–v) and octanethiol-capped (C_8) (samples a–e) silver nanocrystals determined by fitting Eqs. (2)–(4) to the SAXS in Figs. 9(a) and 10(a). The fcc d_{111} spacing, the center-to-center distance C, and the interparticle spacing δ, determined for the corresponding superlattices by indexing the diffraction patterns in Figs. 9(b) and 10(b), are also shown.

Sample	$\bar{R}$ (Å^{-1})	σ	d_{111} (Å)	C (Å)	δ (Å)
i	41	2.8(6.8%)	84.8	97.9	15.9
ii	38.5	2.7(7.0%)	77.2	89.1	12.1
iii	35	3.2(9.1%)	73.6	85.0	15.0
iv	31.5	3.3(10.5%)	68.5	79.1	16.1
v	29	3.3(11.4%)	101.8[a]	72[b]	14[b]
a	25	3.0(12.0%)	51.1	59.0	9.0
b	22	2.5(11.4%)	48.0	55.4	11.4
c	21	2.4(11.4%)	46.5	53.7	11.7
d	20	2.4(12%)	72.8[a]	51.5[b]	11.5[b]
e	18	1.7(9.4%)	$a = 57.4$, $c = 70.0$[c]	49.6[d]	13.6[d]

[a] d_{110} for a bcc superlattice.
[b] Calculated by indexing the first peak in Fig. 9(b) as bcc(110).
[c] Dimensions of the body-centered-tetragonal unit cell determined by indexing the diffraction pattern in Fig. 10(b).
[d] The closest nearest-neighbor distance in the bct superlattice.

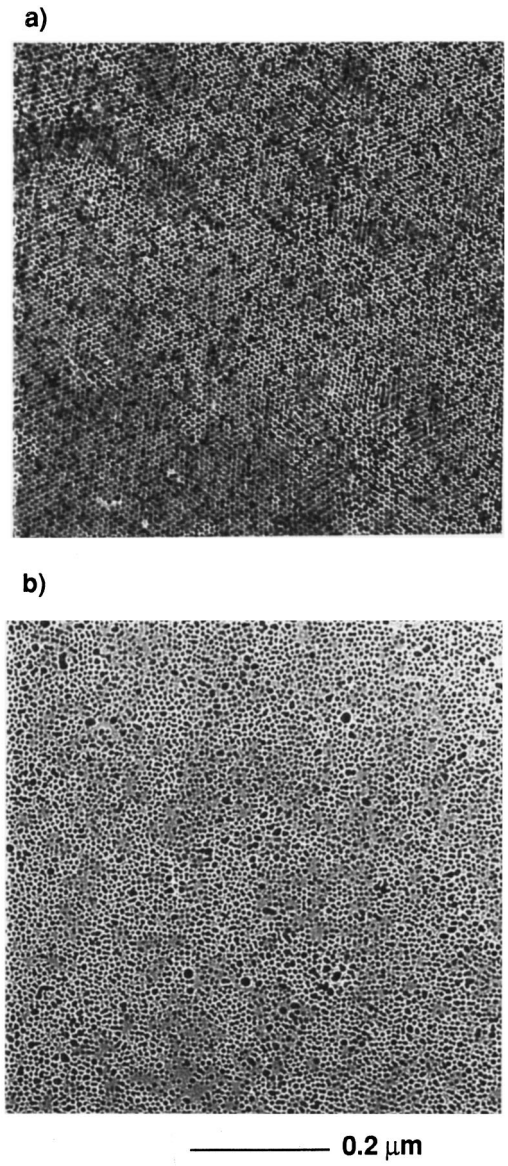

FIG. 4. TEM images of dodecanethiol-capped silver nanocrystals condensed onto carbon substrates showing the difference in superstructure between (a) an ordered monodisperse sample; (b) a disordered polydisperse sample (sample iii and b in Table II, respectively).

$$E_{\text{steric}} \approx \frac{100R\delta_{\text{SAM}}^2}{(C-2R)\pi\sigma_{\text{thiol}}^3} kT \exp\left(\frac{-\pi(C-2R)}{\delta_{\text{SAM}}}\right). \tag{11a}$$

E_{steric} depends on the area occupied by the thiol on the particle surface, σ_{thiol} ($\sigma_{\text{thiol}}=4.3$ Å for dodecanethiol on silver nanocrystals[14]), the length of the capping ligands δ_{SAM} [where δ_{SAM} is taken as the brush thickness of a self-assembled dodecanethiol monolayer, 15 Å (Ref. 43)], and the particle radius R. The strength of the vdW attraction is material dependent and depends on the value of the Hamaker constant A, and can be calculated using the expression[44]

$$E_{\text{vdW}} = -\frac{A}{12}\left\{\frac{4R^2}{C^2-4R^2} + \frac{4R^2}{C^2} + 2\ln\left[\frac{C^2-4R^2}{C^2}\right]\right\}. \tag{11b}$$

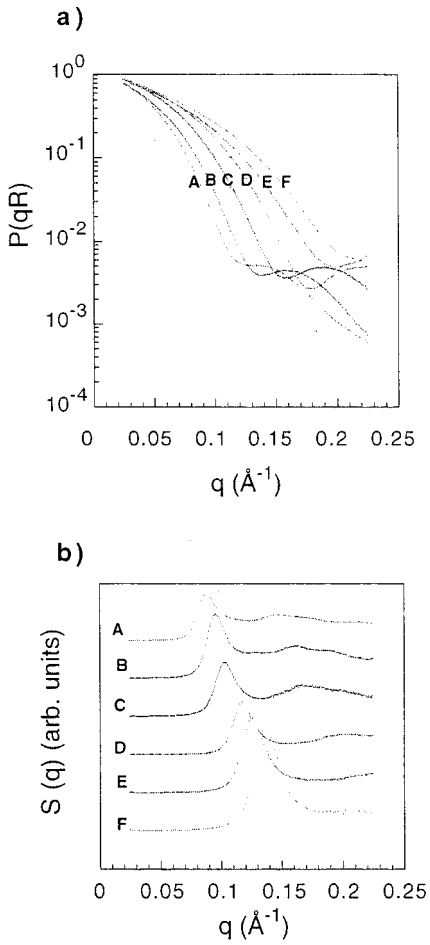

FIG. 5. SAXS measurements of polydisperse C_{12}-capped silver nanocrystals: (a) $P(qR)$ measured from a hexane dispersion, and (b) $S(q)$ measured for spin-coated thin films on mica substrates.

The Lennard-Jones (LJ) potental

$$u(r) = 4\varepsilon\left[\left(\frac{\sigma_{\text{LJ}}}{r}\right)^{12} - \left(\frac{\sigma_{\text{LJ}}}{r}\right)^{6}\right], \tag{12}$$

can also be used as an estimate of $u(r)$. In Eq. (12), σ_{LJ} is the effective hard-sphere diameter and ε is the magnitude of the attractive minimum.

Figure 8 shows the experimentally determined values of $u(r)$ fit with Eqs. (11) and (12). Apart from the oscillations in $u(r)$ in samples A–C, the LJ potential adequately fits the shape of every interparticle potential curve. The corresponding values of σ_{LJ} and ε are shown in Table I. The oscillations may be an artifact of the Fourier-transform method, or they may actually be present, as has been found in liquid metals.[29] Neither Eq. (10), nor the LJ potential, can account for these oscillations in $u(r)$. The most significant deviations between the measured values of $u(r)$ and the model curve fits occur at low r as the effective hard-sphere diameter is approached. This may be due to the particle size distribution in the samples, which would tend to broaden the energetic minimum in $u(r)$. Since a small amount of polydispersity also occurs in the ''monodisperse'' samples that crystallize into superlattices (compare $\pm 8\%$ to $\pm 14\%$), we have neglected the effects of this size distribution on $u(r)$; therefore, the

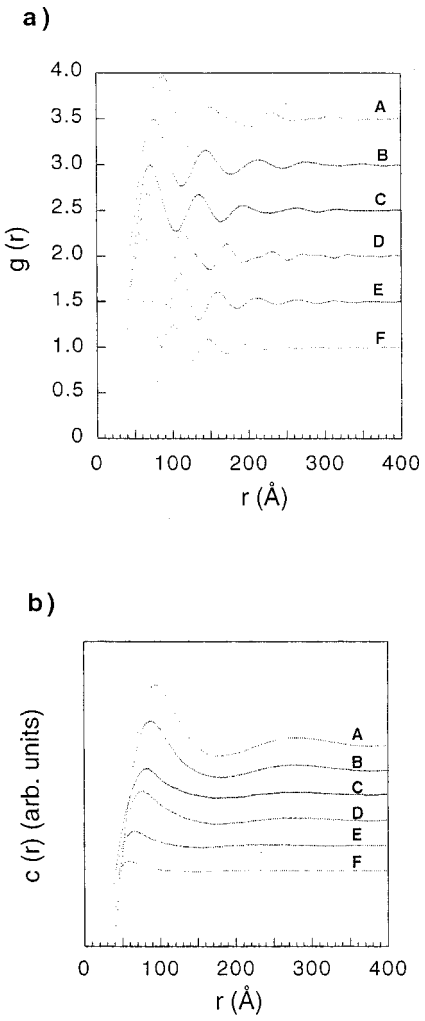

FIG. 6. (a) Radial distribution function and (b) the direct correlation function plotted for samples A–F in Table I. The curves are offset for clarity.

model fit parameters represent ''average'' values for a sample with the given size distribution and average particle radius.

A value of $\delta_{SAM}=15$ Å was initially used for all fits and the best value for A was 7.8 eV for the larger particles, which is about four times greater than the value of 1.95 eV estimated for gold nanocrystals interacting across a hydrocarbon layer.[23] For samples A–C, Eqs. (10) and (11) model the potential quite accurately with these values for δ_{SAM} and A. However, the attractive minimum appears to shift closer to the particle surface with decreased particle diameter, which is counter to what would be expected from Eq. (10) using a constant value of $\delta_{SAM}=15$ Å. In order to fit $u(r)$ for the particles with $\overline{R}<25$ Å using Eq. (10), the values of δ_{SAM} and A decreased significantly.

The apparent decrease in δ_{SAM} for smaller particles might be explained in terms of the very high curvature of the particle surface: even though the thiol ''headgroups'' are close-packed on the particle surface, the chains have a significant amount of freedom further from the particle surface and cannot be considered close-packed.[14] The greater the curvature, the smaller the chain density and therefore, the lower the relative stabilization.

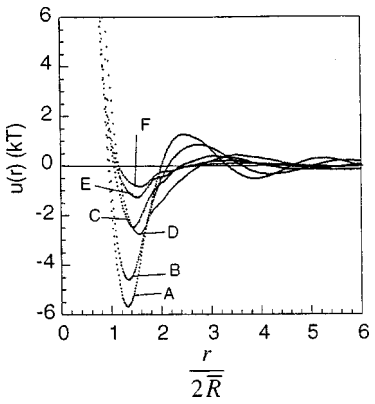

FIG. 7. The pair-interaction potential $u(r)$, calculated using the HNC approximation. Curves A–F correspond to samples A–F in Table I and Figs. 4 and 5.

The range of the repulsion is apparently quite short range and can be modeled as $1/R^{12}$. Interestingly, the repulsion cannot be modeled with a long-range potential like the screened Coulomb potential. Using Eqs. (10) and (11), the steric repulsion, $E_{steric}\propto 1/R^{20}$, is even shorter range than the LJ repulsion and predicts behavior closer to that of hard spheres. The experimentally observed formation of bcc phases of condensed nanocrystal arrays,[8,9] however, does not support hard-sphere behavior and in Fig. 8 it appears that Eq. (10) does not model the repulsion accurately for small nanocrystal core radii. As mentioned above, the smaller nanocrystals have an extreme radius of curvature and the assumption of a tightly-packed monolayer is unlikely to hold.

The importance of the solvent with respect to the interparticle potential cannot be ignored. The interparticle potentials in Figs. 7 and 8 have been determined for *dry* films. The steric stabilization between nanocrystals dispersed in a good solvent, such as hexane, would be stronger than observed for air (a poor solvent). Therefore, the unexpectedly high values for the best fits of A might be attributed as an overcompensation for unreasonably high estimates of E_{steric} calculated using Eq. (10), since it is valid only for good solvents. The interactions between particles in the dry film, however, are the important values to know in order to determine the film structure.[12] In the following section, the usefulness of the LJ parameters determined from the fits of $u(r)$ in Fig. 8 will be demonstrated by calculating the critical value of $\langle L\rangle/R$ for the fcc→bcc phase transition.

C. Solids: Prediction of superlattice packing

The superlattice structure has been found by Whetten and co-workers[8,9] to depend on the ratio of the capping ligand chain length $\langle L\rangle$, to the metal core radius R. Nanocrystals with small $\langle L\rangle/R$ favor fcc packing as would be expected for hard spheres, whereas increased $\langle L\rangle/R$ eventually results in bcc structures. Charge-stabilized colloids analogously favor fcc phases under conditions of high charge screening and bcc phases with low screening and large interparticle separations;[45,46] and qualitatively similar behavior has been found for diblock copolymer micelles in which increased ratios of coronal shell thickness to core radius results in an fcc→bcc phase transition.[31,47] For the charge-stabilized colloids, it has been shown that $u(r)$ is the factor that often

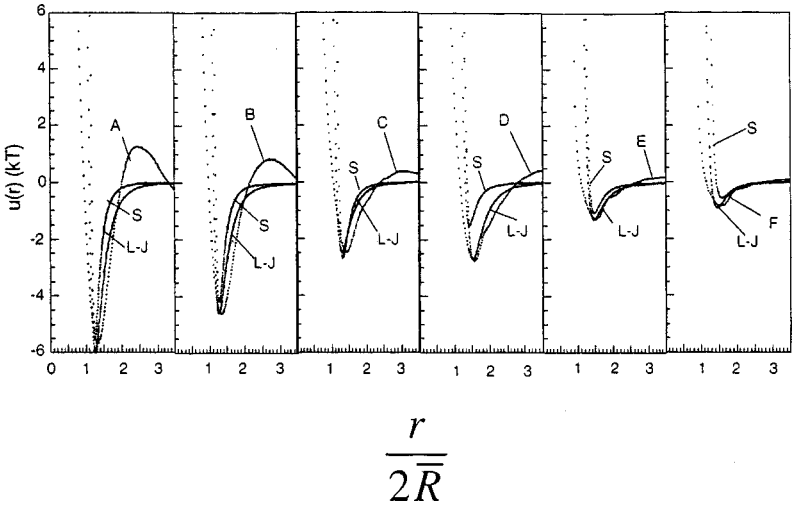

FIG. 8. Curve fits of $u(r)$ from Fig. 5: the data curve is labeled with the sample A–F; the LJ curve fit is labeled with LJ [Eq. (12)]; and the curve fit using Eqs. (10) and (11) using $A=300$ kT and $\delta_{SAM}=15$ Å are labeled as S. The best fit values for A and δ_{SAM} listed in Table II. The LJ parameters σ_{LJ} and ε are shown in Table I for samples A–F.

determines the preferred phase in these systems. For hard-sphere potentials, the fcc phase is always preferred,[21,22] whereas the bcc phase may form under certain conditions when $u(r)$ has a longer range repulsive component, like the Yukawa potential or the inverse power potential r^{-n} with $n<6$.[45,48–51] In contrast, little is understood about the effect of $u(r)$ on the ordering behavior of *sterically* stabilized colloids since the repulsive potentials between particles are seemingly too short-ranged to allow bcc ordering.[51] For example, density-functional theory with $u(r)$ values predicted using self-consistent field calculations, failed to predict the fcc→bcc phase transition for diblock copolymer micelles.[31] Therefore, in the following section, the measured values of $u(r)$ for the nanocrystal systems will be utilized to provide insight into the fundamental nature of the fcc→bcc phase transition.

A series of size-selected monodisperse dodecanethiol- and octanethiol-capped silver nanocrystals were isolated and condensed into thin films on mica substrates. Table II lists $\overline{R}$ and σ for these samples determined by fitting Eqs. (2)–(4) to the $P(qR)$ profiles measured from dilute hexane dispersions shown in Figs. 9(a) and 10(a). The average radii differ between preparations by approximately one lattice plane. The size distributions have σ on the order of $\pm 10\%$ or less.

Figures 9(b) and 10(b) show the SAXS patterns for the condensed nanocrystal films. The diffraction patterns for the larger particles index as fcc superlattices. As the core diameter was decreased, the lattice spacing decreased corresponding to $\overline{R}$ as shown in Table II. The interparticle separation in the superlattices remained constant irrespective of the core particle size, with values of 15 and 11 Å for the dodecanethiol- and octanethiol-capped nanocrystals, respectively. The separation of 1.25 Å/CH_3 means that the interparticle spacing could be tuned with a resolution of less than 2 Å. Below a critical particle size, the diffraction peak positions change and no longer index to an fcc lattice. The smallest dodecanethiol-capped nanocrystals appear to form a bcc lattice. This structure, however, cannot be unambiguously assigned since some splitting in the first-order diffraction peak is evident. However, the octanethiol-capped nanocrystals clearly display a phase transition from fcc to bcc to bct. Estimating the fully extended length $\langle L\rangle$, of the saturated hydrocarbon chain with n atoms as[52]

$$\langle L\rangle=(0.154+0.1265n)\ \text{nm}, \tag{13}$$

the critical values of $\langle L\rangle/R$ for the fcc→bcc phase transition were determined to be 0.59 and 0.60 for dodecanethiol- and octanethiol-capped nanocrystals, respectively.

The progression from fcc to bcc to the more open bct structure with increasing $\langle L\rangle/R$ agrees exactly with what has been observed by Whetten and co-workers[8,9] for alkanethiol-stabilized gold nanocrystals, and the value of $\langle L\rangle/R=0.6$ determined in this study lies well within their proposed packing limits for the bcc phase: $0.4<\langle L\rangle/R<1.0$.[9] However, the observed values of $\langle L\rangle/R$ are slightly less than the approximate value of 0.70 determined by Whetten *et al.*[8,9] The value of $\langle L\rangle/R=0.6$ determined from the data in Figs. 9(b) and 10(b), however, represent a lower limit since the $(110)_{bcc}$ diffraction peaks for samples iv and d show a small degree of peak splitting, which may indicate a mixture of some fcc ordered nanocrystals in the bcc phase. However, decreasing the core radius of the octanethiol-capped nanocrystals further (sample e) gave a distinct superlattice pattern that could only be indexed to a body-centered-tetragonal (bct) phase with a lattice asymmetry, $a/c=1.2$. $\langle L\rangle/R=0.66$ for this sample and represents an *upper* limit for $\langle L\rangle/R$ for a fcc→bcc phase transition for the nanocrystals prepared in this study. Interestingly, the critical value of $\langle L\rangle/R=1.5$ determined by Gast and co-workers[31,45] for diblock copolymer micelles is much different than the values measured for nanocrystals. However, estimating a value for $\langle L\rangle$ as the interparticle spacing in a charge-stabilized colloid array, $\langle L\rangle/R\approx 0.8$ for the fcc→bcc phase transition for these colloids,[45] which interestingly compares quite closely to the critical value of $\langle L\rangle/R$ measured for sterically stabilized nanocrystals.

The values of $u(r)$ measured in the previous section can be used to calculate the difference in free energy between the fcc and bcc phases $\Delta F_{fcc\rightarrow bcc}$. The free energy of the superlattice is a function of the kinetic energy, the binding energy,

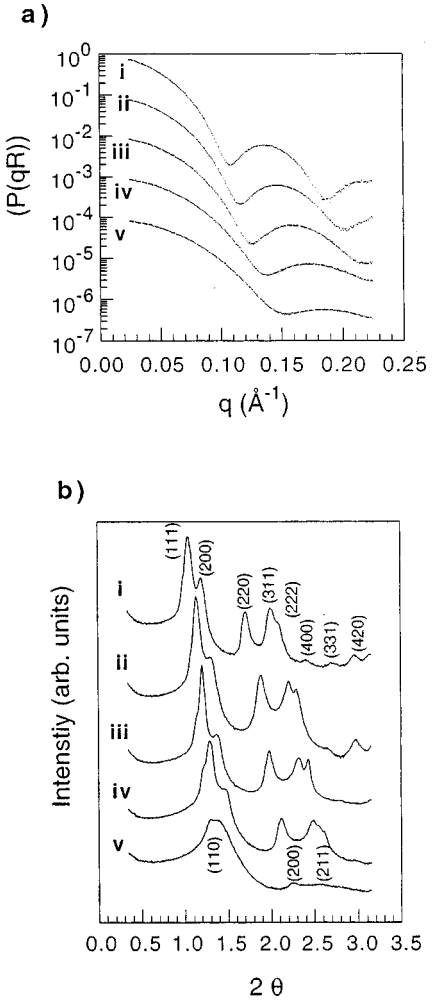

FIG. 9. (a) $P(qR)$ measured by SAXS for a series of dodecanethiol-capped silver nanocrystals dispersed in hexane after size selective precipitation. The curves are offset by a factor of 10, where $P(q=0)=1$. The average particle radius shrinks by approximately one atomic shell per size selection step. (b) SAXS patterns for nanocrystal thin films spin-coated onto mica substrates. The corresponding average particle diameter and d_{111} spacing are listed in Table II.

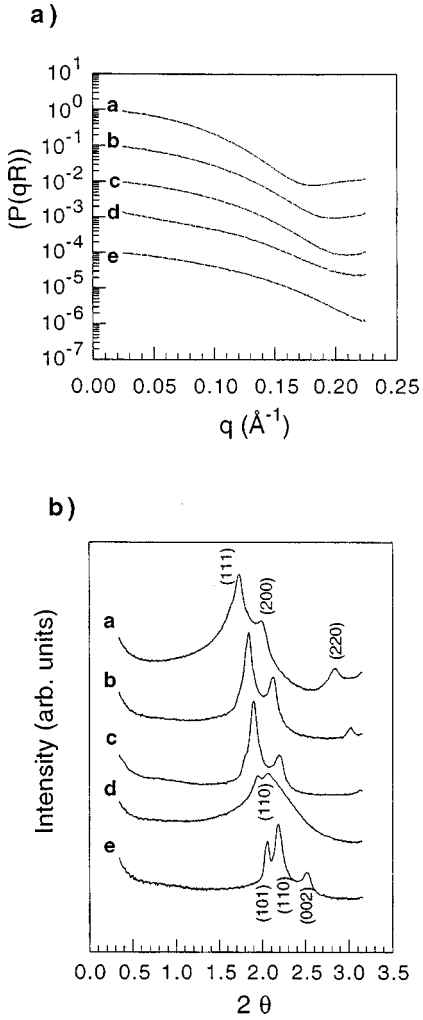

FIG. 10. (a) $P(qR)$ measured by SAXS for a series of octanethiol-capped silver nanocrystals dispersed in hexane after size selective precipitation. The curves are offset by a factor of 10, where $P(q=0)=1$. The average particle radius shrinks by approximately one atomic shell per size selection step. (b) SAXS patterns for nanocrystal thin films spin coated onto mica substrates. The corresponding average particle diameter and d_{111} spacing are listed in Table II.

and the entropy in the lattice. $\Delta F_{\mathrm{fcc}\rightarrow\mathrm{bcc}}$ can be expressed solely in terms of the differences in binding energy ΔE, and entropy ΔS,

$$\Delta F_{\mathrm{fcc}\rightarrow\mathrm{bcc}}=\Delta E-T\Delta S, \tag{14}$$

since the kinetic energy term cancels.[48]

The binding energy U, for the two superlattice structures can be calculated explicitly using the LJ parameters listed in Table I:[53]

$$U=2\varepsilon\left[A_{12}\left(\frac{\sigma_{\mathrm{LJ}}}{r}\right)^{12}-A_6\left(\frac{\sigma_{\mathrm{LJ}}}{r}\right)^{6}\right], \tag{15}$$

where r is the interparticle spacing in the lattice and A_n depends on the crystal structure. For the 6-12 LJ potential, $A_{12,\mathrm{fcc}}=12.13$, $A_{12,\mathrm{bcc}}=9.11$, $A_{6,\mathrm{bcc}}=12.25$, $A_{6,\mathrm{fcc}}=14.45$.[53] The difference in the binding energy per nanocrystal between the bcc and fcc phases gives the energy difference $\Delta E_{\mathrm{fcc}\rightarrow\mathrm{bcc}}$. Unlike the case for the charge-stabilized colloids with $u(r)$ that can be modeled with a screened Coulomb potential in which the fcc phase is favored with high screening, and the bcc phase is favored for low screening (i.e., the Wigner lattice[54,55]), the sterically stabilized nanocrystals with the experimentally determined shorter range repulsive potentials, always *energetically* favor the higher coordination phase—fcc.

The entropy difference between the two phases can be estimated by expanding the partition function, assuming a harmonic system with $3N$ degrees of freedom at temperatures above the highest normal mode frequency: $\Delta S \cong 3Nk\ln(\omega_E/\omega_E')$.[48,56] Friedel[57] has argued that the ratio of the effective ''Einstein frequencies,'' ω_E/ω_E', can be estimated with a nearest-neighbor central force model to give $\Delta S_{\mathrm{fcc}\rightarrow\mathrm{bcc}}=0.61NkT$. Therefore, the entropy difference always favors the more open bcc structure.

Figure 11 shows $\Delta F_{\mathrm{fcc}\rightarrow\mathrm{bcc}}$ calculated as a function of $\langle L\rangle/R$ using the experimentally measured LJ parameters listed in Table I. The size polydispersity in these samples

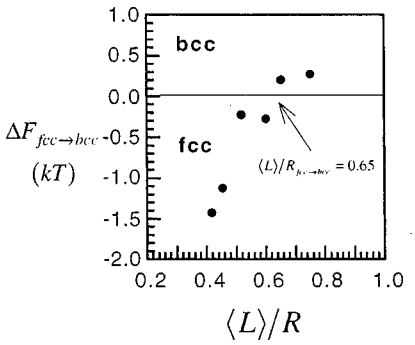

FIG. 11. The free-energy difference between the fcc and bcc superlattice structures $\Delta F_{\mathrm{fcc}\rightarrow\mathrm{bcc}}$ (●), calculated as a function of $\langle L\rangle/R$ using Eqs. (13)–(15) and the experimentally determined values of $u(r)$ for dodecanethiol-capped silver nanocrystals.

was not accounted for in the calculations.[58] As $\langle L\rangle/R$ increases, the tendency to form a bcc superlattice increases until a critical value of $\langle L\rangle/R\approx 0.65$ is reached. For $\langle L\rangle/R \lesssim 0.65$, the bcc phase is most stable. This is surprisingly close to the value determined experimentally by both our group and Whetten *et al.*[8,9] Therefore, based on these calculations, it would appear that it is the ''macroscopic'' attractive and entropic forces that drive the fcc→bcc phase transition. This contrasts with the idea proposed by Leudtke and Landman and co-workers[8,9,25] that the ''microscopic'' chain interactions are solely responsible for the observed fcc→bcc phase transition for alkanethiol-stabilized gold and silver nanocrystals. However, the lower symmetry bct superlattice formed by high $\langle L\rangle/R$ octanethiol-capped silver nanocrystals in this study (sample e) is qualitatively consistent with predictions made by Leudtke and Landman and co-workers[8,9,25] and seems to indicate that the chain-chain interactions do (at least partially) affect superlattice ordering. Therefore, the $\langle L\rangle/R$ dependence on the fcc→bcc phase transition appears to result from a combination of ''macroscopic'' and ''microscopic'' effects, and the capping ligands serve either as space fillers, or may contribute to some portion of binding energy, or stabilization energy, of the superlattice. Microscopic probes which could illuminate the chain configurations in the superlattice should provide the needed evidence to show how the chains contribute to nanocrystal ordering.

IV. CONCLUSION

In this paper, a conceptually unique approach to the measurement of $u(r)$ between thiol-stabilized nanocrystals has been developed. By incorporating a small size distribution in the nanocrystal sample, condensed films of these particles do not exhibit ordering, and can thus be treated as dense fluids. Using SAXS, both $P(qR)$ and $S(q)$, were measured. $S(q)$ for the disordered films were used to calculate the pair interparticle potential $u(r)$ as a function of the ratio of the capping ligand chain length to the core nanocrystal radius $\langle L\rangle/R$. These calculations relied on the accuracy of the hypernetted chain (HNC) approximation at very high fluid densities and any error associated with the use of this integral equation comes from the fundamental difficulties related to the study of dense fluids, and does not reflect the adequacy of the experimental approach. $u(r)$ could be modeled using an expression for steric repulsion derived by de Gennes[40–42] for larger particles, but appears to break down for smaller particles, most likely due to the extreme curvature of the nanocrystal surface. All of the $u(r)$ curves could be fit with the 6-12 Lennard-Jones potential, indicating a relatively short-range repulsion for all particle sizes.

The fcc→bcc phase transition was observed for both dodecanethiol- and octanethiol-capped silver nanocrystals at $\langle L\rangle/R=0.60$. The octanethiol-capped silver nanocrystals exhibit bct packing at $\langle L\rangle/R>0.66$. The experimentally determined values of $u(r)$ were used in conjunction with a simple model for $\Delta F_{\mathrm{fcc}\rightarrow\mathrm{bcc}}$, which predicted the fcc→bcc phase transition to occur at $\langle L\rangle/R=0.65$. This value corresponds quite closely to the experimental values observed in this study, as well as the values measured by Whetten and co-workers.[8,9] In short, it appears that the ''macroscopic'' attraction between particles and the ordering entropy in the superlattice are certainly important to the superlattice structure.

ACKNOWLEDGMENTS

The authors thank S. Fullam, S. Connolly, and D. Aherne for their insightful comments; D. Cottell and B. Cregg for their assistance at the University College Dublin electron microscopy laboratory; and E. Komanschek at the Central Laboratory of the Research Councils, Daresbury. We also thank the Commission of the European Union for funding access to the synchrotron-radiation source at this laboratory through the Large Scale Facilities Program.

*Present Address: Department of Chemical Engineering and the Texas Materials Institute, The University of Texas at Austin, Austin, TX 78712-1062.

†Author to whom correspondence should be addressed.

[1] M. D. Bentzon, J. van Wonterghem, S. Morup, A. Tholen, and C. J. W. Koch, Philos. Mag. B **60**, 169 (1989).

[2] C. B. Murray, C. R. Kagan, and M. G. Bawendi, Science **270**, 1335 (1995).

[3] C. R. Kagan, C. B. Murray, and M. G. Bawendi, Phys. Rev. B **54**, 8633 (1996).

[4] R. P. Andres, J. D. Bielefeld, J. I. Henderson, D. B. Janes, V. R. Kolagunta, C. P. Kubiak, W. J. Mahoney, and R. G. Osifchin, Science **273**, 1690 (1996).

[5] S. A. Harfenist, Z. L. Wang, M. M. Alvarez, I. Vezmar, and R. L. Whetten, J. Phys. Chem. **100**, 13 904 (1996).

[6] R. L. Whetten, J. T. Khoury, M. M. Alvarez, S. Murthy, I. Vezmar, Z. L. Wang, P. W. Stephens, C. L. Cleveland, W. D. Luedtke, and U. Landman, Adv. Mater. **8**, 428 (1996).

[7] S. A. Harfenist, Z. L. Wang, R. L. Whetten, I. Vezmar, and M. M. Alvarez, Adv. Mater. **9**, 817 (1997).

[8] R. L. Whetten (private communication).

[9] R. L. Whetten, M. N. Shafigullin, J. T. Koury, T. G. Schaaff, I.

Vezmar, M. M. Alvarez, and A. Wilkinson, Acc. Chem. Res. (to be published).
[10] L. Motte, F. Billoudet, E. Lacze, J. Douin, and M. P. Pileni, J. Phys. Chem. B **101**, 138 (1997).
[11] S. Connolly, S. Fullam, B. Korgel, and D. Fitzmaurice, J. Am. Chem. Soc. **120**, 2969 (1998).
[12] B. A. Korgel and D. Fitzmaurice, Phys. Rev. Lett. **80**, 3531 (1998).
[13] B. A. Korgel and D. Fitzmaurice, Adv. Mater. **10**, 661 (1998).
[14] B. A. Korgel, S. Fullam, S. Connolly, and D. Fitzmaurice, J. Phys. Chem. B **102**, 8279 (1998).
[15] J. S. Yin and Z. L. Wang, Phys. Rev. Lett. **79**, 2570 (1997).
[16] For recent reviews, see A. P. Alivisatos, Science **271**, 933 (1996); G. Schmid, Chem. Rev. **92**, 1709 (1992); J. Schi, S. Gider, and D. D. Awschalom, Science **271**, 937 (1996).
[17] R. P. Feynman, *Statistical Mechanics* (Benjamin, Reading, MA, 1972).
[18] D. A. McQuarrie, *Statistical Mechanics* (Harper & Row, New York, 1976).
[19] See, for example, P. N. Pusey, W. C. K. Poon, S. M. Ilett, and P. Bartlett, J. Phys.: Condens. Matter **6**, A29 (1994).
[20] P. N. Pusey and W. van Megen, Nature (London) **320**, 340 (1986).
[21] B. J. Alder, and T. E. Wainwright, J. Chem. Phys. **27**, 1208 (1957).
[22] B. J. Alder, W. G. Hoover, and D. A. Young, J. Chem. Phys. **49**, 3688 (1968).
[23] P. C. Ohara, D. V. Leff, J. R. Heath, and W. M. Gelbart, Phys. Rev. Lett. **75**, 3466 (1995).
[24] J. R. Heath, C. M. Knobler, and D. V. Leff, J. Phys. Chem. B **101**, 189 (1997).
[25] W. D. Luedtke and U. Landman, J. Phys. Chem. **100**, 13 323 (1996).
[26] O. Glatter and O. Kratky, *Small Angle X-ray Scattering* (Academic, New York, 1982).
[27] H. Mattoussi, A. W. Cumming, C. B. Murray, M. G. Bawendi, and R. Ober, J. Chem. Phys. **105**, 9890 (1996).
[28] R. H. Ottewill, in *Colloidal Dispersions*, edited by J. W. Goodwin (Royal Society of Chemistry, London, 1982).
[29] J. P. Hansen and I. R. MacDonald, *Theory of Simple Liquids* (Academic, London, 1976).
[30] See, for example, D. Stirpe and C. W. Tompson, J. Chem. Phys. **36**, 392 (1962).
[31] G. A. McConnell and A. P. Gast, Phys. Rev. E **54**, 5447 (1996).
[32] J. D. Weeks, Philos. Mag. **35**, 1345 (1977).
[33] R. Hasegawa, *Glassy Metals: Magnetic Chemical and Structural Properties* (CRC, Boca Raton, FL, 1983).
[34] P. A. Monson (private communication).
[35] W. M. Gelbart and A. Ben-Shaul, J. Phys. Chem. **100**, 13 169 (1996).
[36] M. Brust, M. Walker, D. Bethell, D. J. Schiffrin, and R. Whyman, J. Chem. Soc. Chem. Commun. 801 (1994).
[37] M. Kerker, *The Scattering of Light and other Electromagnetic Radiation*: (Academic, New York, 1969).
[38] M. O. Robbins, K. Kremer, and G. S. Grest, J. Chem. Phys. **88**, 3286 (1988).
[39] F. J. Rogers and D. A. Young, Phys. Rev. A **30**, 999 (1984); H. S. Kang and F. H. Ree, J. Chem. Phys. **103**, 3629 (1995).
[40] C. de Gennes, R. Acad. Sci. (Paris) **300**, 839 (1985); Adv. Colloid Interface Sci. **27**, 189 (1987).
[41] B. V. Derjaguin, Kolloid-Z. **69**, 155 (1934).
[42] J. N. Israelachvili, *Intermolecular and Surface Forces*, 2nd ed. (Academic, New York, 1992).
[43] M. D. Porter, T. B. Bright, D. L. Allara, and C. E. D. Chidsey, J. Am. Chem. Soc. **109**, 3559 (1987).
[44] H. C. Hamaker, Physica (Amsterdam) 1058 (1937).
[45] Y. Monovoukas and A. P. Gast, J. Colloid Interface Sci. **128**, 533 (1989).
[46] See, for example, R. Williams and R. S. Crandall, Phys. Lett. **48A**, 225 (1974).
[47] G. A. McConnell, A. P. Gast, J. S. Huang, and S. D. Smith, Phys. Rev. Lett. **71**, 2102 (1993).
[48] P. M. Chaikin, P. Pincus, S. Alexander, and D. Hone, J. Colloid Interface Sci. **89**, 555 (1982).
[49] J. M. Silva and B. J. Mokross, Phys. Rev. B **21**, 2972 (1980).
[50] W. Y. Shih, W. A. Aksay, and R. Kikuchi, J. Chem. Phys. **86**, 5127 (1987).
[51] W. G. Hoover, D. A. Young, and R. Grover, J. Chem. Phys. **56**, 2207 (1972).
[52] C. Tanford, *The Hydrophobic Effect* (Wiley, New York, 1980).
[53] C. Kittel, *Introduction to Solid State Physics*, 5th ed. (Wiley, New York, 1976); N. W. Ashcroft and N. D. Mermin, *Solid State Physics*, international ed. (Reinhart and Winston, New York, 1976).
[54] L. L. Foldy, Phys. Rev. B **3**, 3472 (1971).
[55] K. Fuchs, Proc. R. Soc. London, Ser. A **151**, 585 (1935).
[56] L. D. Landau and E. M. Lifschitz, *Statistical Physics*, 3rd ed. (Pergamon, New York, 1980).
[57] J. Friedel, J. Phys. (France) Lett. **35**, L-59 (1974).
[58] As mentioned above, the LJ parameters determined for the polydisperse samples listed in Table I represent ''average'' values for those samples. Therefore, the fact that real samples have a narrow (yet finite) size distribution is somewhat reflected in the calculated values of $\Delta F_{\mathrm{fcc}\rightarrow\mathrm{bcc}}$. Since the size distributions of the polydisperse and monodisperse samples differ by only $\sim$5%, the parameter values were not corrected to account for these minimal differences.